HiSST: 3rd International Conference on
High-Speed Vehicle Science Technology
14 -19 April 2024, Busan, Korea

Aerodynamics of the Reusable Launch Vehicle Supersonic Retropropulsion System

Jesslyn Wei Yan Ong [1], Yujoo Kang [2], Jaemyung Ahn [3], Sang Lee [4]

Abstract

Reusable Launch Vehicle (RLV) has validated the Vertical Take-off and Vertical Landing (VTVL) reusable rocket concept through the implementation of a robust vehicle design tailored to the well-structured mission profile executed in distinct phases, varying in altitude and travel speed. This study performs an in-depth exploration of the flowfield attributes and comprehensive aerothermal analyses of the vehicle and the surrounding atmosphere. The employment of the Reynolds Averaged Navier-Stokes (RANS) solver in conjunction with the Spalart-Allmaras (SA) model within SU2 was instrumental in conducting these analyses. The findings reveal that as the vehicle progresses to lower speeds and altitudes, the manifestation of shock and plume formation becomes less pronounced, consequently diminishing the associated aerothermal effects.

Keywords: Computational fluid dynamics, Supersonic flow, Reusable launch vehicle, Supersonic retropropulsion

Nomenclature

h – Altitude

ρ – Density

T – Temperature

p – Pressure

M – Mach number

v – Velocity

AOA – Angle of attack

[1] *Korea Advance Institute of Science and Technology, 291 Daehak-ro, Yuseong-gu, 34141 Daejeon, Republic of Korea, jesslynong24@kaist.ac.kr*
[2] *Korea Advance Institute of Science and Technology, 291 Daehak-ro, Yuseong-gu, 34141 Daejeon, Republic of Korea, ky5731@kaist.ac.kr*
[3] *Korea Advance Institute of Science and Technology, 291 Daehak-ro, Yuseong-gu, 34141 Daejeon, Republic of Korea, jaemyung.ahn@kaist.ac.kr*
[4] *Korea Advance Institute of Science and Technology, 291 Daehak-ro, Yuseong-gu, 34141 Daejeon, Republic of Korea, slee1@kaist.ac.kr*

1. Introduction

Reusable Launch Vehicles (RLVs) have become a focal point in space exploration due to their potential to reduce costs significantly. By implementing efficient re-entry procedures, launched vehicles can be inspected and refurbished for multiple uses, thus cutting down on manufacturing expenses. In recent years, there has been a surge of interest in RLV technology from various countries, companies, and individuals worldwide. Among these initiatives, SpaceX's Falcon 9 stands out as one of the most notable Vertical Take-off Vertical Landing (VTVL) RLVs. According to SpaceX's data as of October 2023, Falcon 9 has completed an impressive 261 launches, with 219 successful landings and 194 reflight occurrences.

During the re-entry procedure, encounter various altitudes and speeds along their mission trajectory. To ensure optimal vehicle design and accurately predict aerodynamic properties, it's crucial to conduct aerodynamic analyses under different flow conditions. In recent years, numerous studies on RLVs have been conducted, covering a wide range of topics. Ecker et al. examined the thermal load experienced by Falcon 9 during supersonic retro-propulsion (SRP) maneuvers. Their study highlighted how the plume envelope affects the vehicle at different points along its trajectory, leading to the formation of shocks and changes in heat flux. As the vehicle descends to lower speeds and altitudes, the plume envelope reduces in size until it no longer interacts with the vehicle's body. In addition, Kim et al. delved into aerodynamic analysis during the freefall phase of Falcon 9, exploring characteristics at various altitudes and Mach numbers. They also investigated the impact of adjusting vehicle thrust values during the landing burn. Their findings revealed a significant reduction in shock formation as travel speed and altitude decreased.

In the stage of supersonic retro-propulsion (SRP), the exhaust plume creates a bow shock upstream and induces the high thermal effect and high-frequency pressure loads. It damages structures and actuators which leads a failure of the system in extreme case. Marwege et al. [6] conducted tests on the two-stage-to-orbit (TSTO) RETAL1 in the Hypersonic Wind Tunnel Cologne under hypersonic retro-propulsion conditions with Mach number 5.3 and 7.0. Their experiment compared single-engine and three-engine retro-propulsion flows under different test conditions, including variations in exhaust temperature (hot and cold exhaust). They analyzed flow properties across the centerline from the bow shock to the Mach disk.

However, there is a notable gap in literature concerning re-entry plume-shock interaction across various trajectory point under varying flow conditions. In this study, the comprehensive aerodynamic analysis of two key segments of the mission are conducted: the freefall manoeuvre and the re-entry burn phase. Specifically, this study delves into the intricate interactions between the moving body and the phenomena of shock and plume formation during the re-entry burn. Furthermore, an in-depth aerothermal analysis is conducted around the vehicle to unravel the complex thermochemical reactions occurring between the plume and the supersonic atmospheric flow conditions.

2. Descent Profile

The descent profile of Falcon 9 from the peak altitude typically comprises three distinct phases including the freefall manoeuvre, entry burn and landing burn as shown in Fig. 1. While Table 1 features the descent profile re-examined for this investigation which is based on the Falcon 9 NROL-76 mission took place on 1st of May 2017.

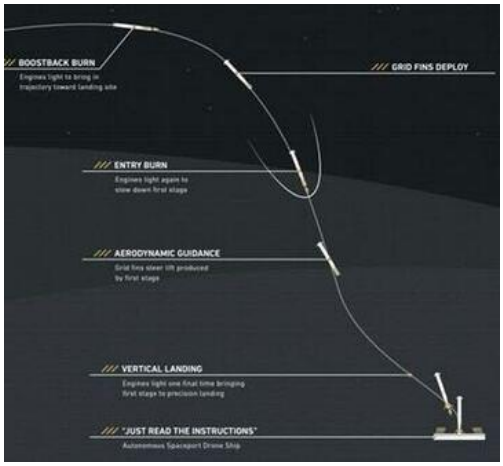

Fig. 1: Falcon 9 descend profile [5]

Upon reaching the apogee at an altitude of 166 kilometres, the descent phase is initiated, marking a critical transition in the vehicle's trajectory. At this phase, the vehicle undergoes aerodynamic freefall, with no engine ignition to counteract the gravitational pull. Descending further to an altitude of 68.4 kilometres, the vehicle transitions into the entry burn process, a key stage where three engines ignite to initiate deceleration. The abrupt activation of engines generates a significant shock wave, indicative of the high-speed deceleration experienced by the vehicle. Concurrently, the formation of a plume and subsequent interaction with the shock wave exemplify a non-equilibrium flow regime, highlighting the complex aerodynamic conditions. However, this ignition sequence is short-lived, lasting a mere 26 seconds before the engines are extinguished. Subsequently, the vehicle is steered towards the designated landing zone, where preparations for touchdown commence. As the vehicle gradually approaches the ground, it enters the final landing burn process, wherein only one centre nozzle is ignited to execute the last phase of deceleration before touchdown, ensuring a safe and controlled landing.

Table 1: NROL-76 mission profile [8]

Mission	Time, s	Altitude, km	Velocity, m/s
Apogee	288	166	290
Descending	319	160	422
	359	140	744
	384	120	963
	404	100	1143
	421	80	1303
Entry burn start	430	68.4	1385
Entry burn	436	60	1391
	444	50	1154
	455	40	784
Entry burn end	456	39.2	751
Landing burn	508	5	325
Landing	540	0	6

3. Methodology

I. Geometry and boundary conditions

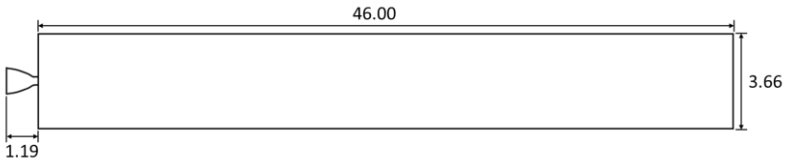

Fig. 2: Simplified geometry of Falcon 9 with single nozzle. Dimensions in metres.

In accordance with the Falcon 9 configurations outlined by SpaceX in 2021 [5], with the additional reference to the geometry proposed by Ecker et al. [2], a simplified 2-Dimensional geometry of the Falcon 9 rocket was constructed for this study. The geometry features total dimensions of 3.66 meters in diameter and 47.09 meters in length, with the nozzles shaped according to a second-order polynomial function, r(x) = -0.187051x^2 + 0.532439x + 0.119. For the purposes of this paper, as shown in Fig. 2, only the centre nozzle was considered, and the nozzle exit was sealed in the analysis.

The boundary conditions for the extremities of the computational domain were assigned as far-field boundary conditions, while the vehicle itself was treated as an isothermal wall at 300 K. In the condition with the engine ignition, the nozzle exit was simulated with the respective exhaust flow, and the temperature of the nozzle wall was set to 1000 K.

II. Gas Model

A standard air model (77% N_2 and 23% O_2) was employed in the analyses according to the standard atmospheric condition at desired altitude from Table 3. At the nozzle exit, a mass flow of exhaust gas was computed based on the engine model proposed by Ecker et al. [2], which drew upon estimations from the NASA Chemical Equilibrium with Applications (CEA) tool. The properties of the exhaust gas were reviewed to accommodate the requirement of the analyses as shown in Table 2. The gas model was considered as a chemically nonreacting perfect gas throughout the simulations.

Table 2: Nozzle flow parameters

Exhaust gas parameters			
ρ (kg/m3)	T (K)	u (m/s)	p (kPa)
0.119	1250	3000	42.70

Species	Mass fraction	
	Ecker et al. [2]	Adapted in this paper
CO	3.9547E-1	4.1802E-1
CO_2	9.7310E-2	9.7467E-2
COOH	1.7644E-5	-
H	2.2984E-2	2.3022E-2
HCO	4.7436E-5	-
HO_2	1.3580E-5	-
H_2	1.5024E-1	1.5048E-1
H_2O	3.0706E-1	3.0755E-1
O	1.9350E-3	1.9385E-3
OH	2.3384E-2	-
O_2	1.5200E-3	1.5225E-3

III. Numerical method

The Computational Fluid Dynamics (CFD) analyses were performed using SU2, an open-source Multiphysics simulation and design software [4]. The simulation model incorporated steady-state

Reynolds Averaged Navier-Stokes (RANS) solver, accompanied by the Spalart-Allmaras (SA) model. The initial condition was configured to replicate standard atmospheric conditions at corresponding altitudes, adhering to the air viscosity by the Sutherland's Law.

The second-order spatial discretisation was achieved using the weighted least squares spatial gradients method combined with Monotonic Upstream-centred Scheme for Conservation Laws (MUSCL) scheme. The Advection Upstream Splitting Method (AUSM) was applied to discretise the convective fluxes. The time discretisation was then achieved using the pseudo implicit Euler method.

The simulations were conducted in accordance with the specifications outlined in Table 3, encompassing thorough analyses of both regions with and without engine ignition. This meticulous examination enabled a detailed understanding of the vehicle's behaviour under varying conditions, offering valuable insights into the impact of engine ignition on descent dynamics and overall performance.

Table 3: Conditions of interest

Plume interaction	Altitude (km)	T_∞ (K)	ρ_∞ (kg/m^3)	p_∞ (Pa)	V (m/s)
No	90	187.21	2.93E-06	0.15	1227
	80	198.64	1.85E-05	1.05	1303
	70	219.58	8.28E-05	5.22	1374
Yes	68.4	223.97	1.03E-04	6.65	1385
	39.2	248.14	4.49E-03	319.99	751

IV. Mesh configuration

Within the paper, multiple mesh configurations were applied satisfying specific demand of each cases. To achieve high precision of the outcomes, y+ value of each meshes approximates to 1 in an unstructured manner.

4. Results

4.1 Freefall phase

Fig. 3 presents the flowfield of the launch vehicle during the first freefall phase from 70km to 90km where the launch vehicle descends after reaching its peak height prior to entry burn phase.

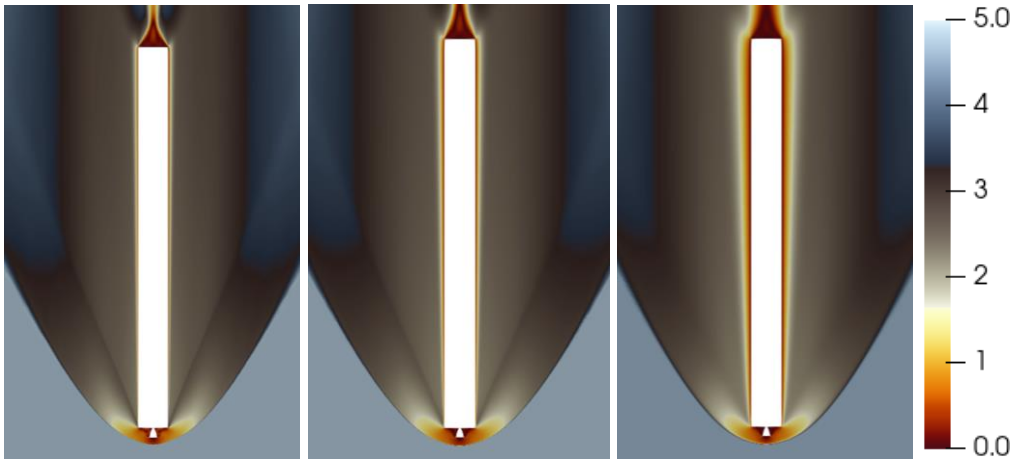

(a) 70 km - M 4.625 (b) 80 km - M 4.613 (c) 90 km - M 4.475

Fig. 3: Freefall flowfield

During this phase, the vehicle undergoes freefall during which the engine is not ignited to decelerate. It is generally acknowledged that as the altitude decreases, the vehicle experiences an escalating drag

force due to the increasing dynamic pressure along its re-entry trajectory. This statement is further supported by a similar investigation conducted by Kim., Y. et al. (2021) [3].

From Fig. 3, it is evident that bow shock forms beneath the descending vehicle. Additionally, due to the presence of sharp edges in the proposed geometry, normal shock is observed extending out from the sharp edges. As the Mach number increases, the dimension of the shock decreases in which the shock wave is more attached to the body. The formation of bow shock beneath the nozzle results in the heating of the region around the nozzle and the baseplate of the vehicle, as evidenced by the analysis of wall heat fluxes. This observation highlights the significant thermal effects induced by the aerodynamic interactions during descent.

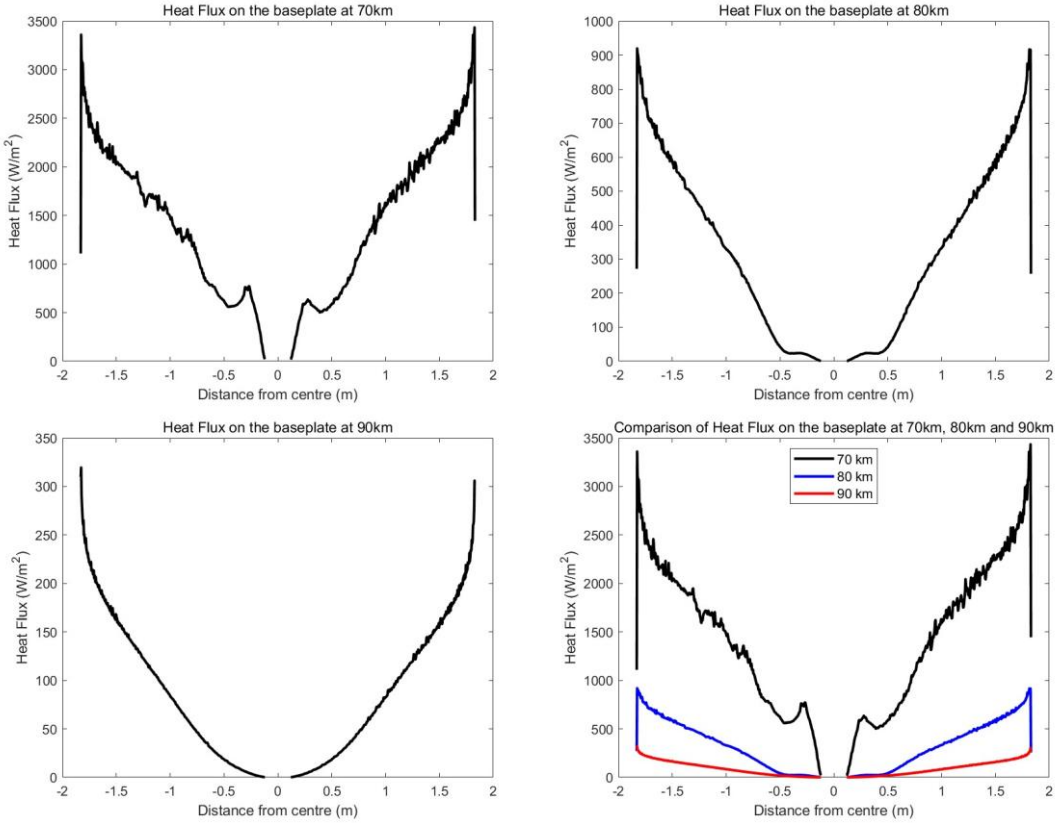

Fig. 4: Heat Flux on the baseplate

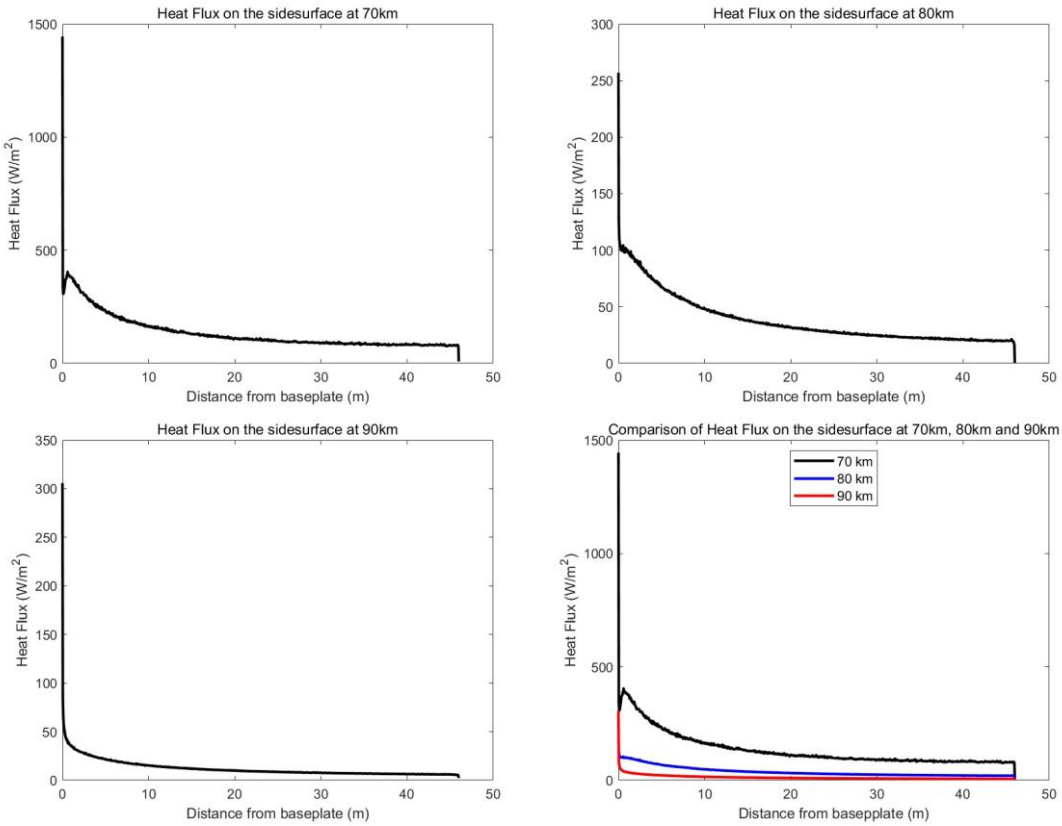

Fig. 5: Heat Flux on the side surface

Besides, recirculation zone is found in the region between the nozzle and the baseplate. This can be seen as the cause of baseplate heating as when the high temperature reverse flow propagates in the recirculation zone as shown in Fig. 6, the baseplate is exposed to high convective heating. As the Mach number increases, the heating effect is more significant, leading to greater heat flux count. In addition, the sidewall is also exposed to severe convective heating especially near the baseplate.

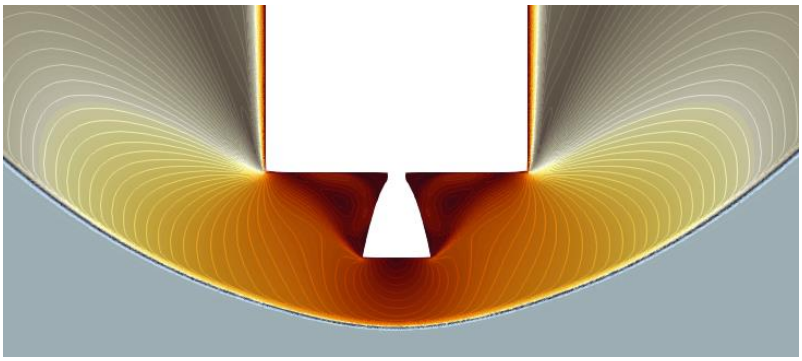

Fig. 6: Flow circulation around the nozzle

4.2 Plume-shock interaction

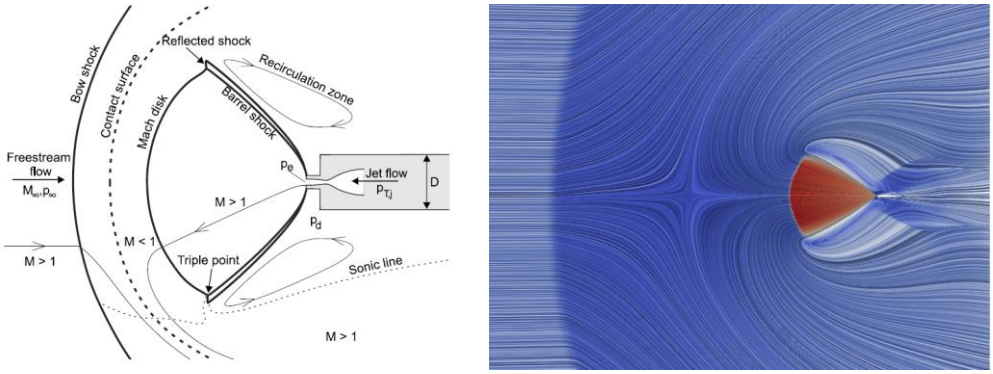

Fig. 7: Expected flowfield [7] (left) vs. snapshot of initial flowfield in this paper (right)

Fig. 7 illustrates the instantaneous flowfield of the plume-shock interaction when the freestream flow confronts with exhaust gas spouting out from the nozzle. Based on Fig. 7, the flow features observed agreed with the flow features diagram proposed by Marwege et al [7]. Due to the presence of the exhaust plume, bow shock was formed at a shock stand-off distance ahead of the nozzle exit plane. The Mach disk was clearly observed surrounded by the barrel shock, resulting in a triple point intersection. As the exhaust flow propagated in the opposite direction of the freestream flow, the exhaust flow recirculated towards the vehicle and thus a recirculation zone was formed around the region near the barrel shock. Between the bow shock and the Mach disk, the freestream flow deflects after passing through the bow shock against the incoming exhaust flow, forming a contact surface as observed from Fig. 7.

5. Conclusion

This study aims to investigate the effect of engine ignition towards the Falcon 9 body due to the plume-shock interaction that leading to having a non-equilibrium regime around the vehicle. Therefore, aerodynamic analysis of a simplified Falcon 9 model with a single nozzle is performed to obtain deeper insights on the flow features around the vehicle.

During the freefall phase where the vehicle descends with increasing speed along the atmosphere with decreasing density, the dimension of the shock decreases along the trajectory. The bow shock becomes more attached to the body with decreasing shock stand-off distance. Additionally, the reduction in boundary layer thickness is as well observed with the decreasing altitude. Along the descent trajectory, the thermal effect on the wall of the vehicle is highlighted where the heat effect concentrates on the baseplate of the vehicle, extending along the sidewall due to the presence of reverse freestream flow.

Under the condition where engine ignition does not occur, the thermal load on the baseplate is less significant compared to the condition where plume-shock interaction occurs.

References

1. SpaceX: Falcon 9. SpaceX. https://www.spacex.com/vehicles/falcon-9/ (2023). Accessed 13 October 2023
2. Ecker, T., Karl, S., Dumont, E., Stappert, S., Krause, D.: Numerical Study on the Thermal Loads During a Supersonic Rocket Retropropulsion Maneuver. Journal of Spacecraft and Rockets, 57(1), 131-146. https://arc.aiaa.org/doi/epdf/10.2514/1.A34486 (2020). Accessed 13 October 2023
3. Kim, Y., Lee, H., Roh, T.: Analysis of Propellant Weight under Re-entry Conditions for a Reusable Launch Vehicle Using Retropropulsion. Energies. https://doi.org/10.3390/en14113210 (2021). Accessed 13 October 2023
4. Economon, T.D., Palacios, F., Copeland, S.R., Lukaczyk, T.W., Alonso, J.J.: SU2: An open-source suite for multiphysics simulation and design. AIAA Journal, 54(3), 828-846. https://arc.aiaa.org/doi/10.2514/1.J053813 (2016) Accessed 13 October 2023
5. SpaceX: Falcon User's Guide. SpaceX. https://www.spacex.com/media/falcon-users-guide-2021-09.pdf (2021). Accessed 13 October 2023
6. Marwege, A. and Gülhan, A.: "Unsteady Aerodynamics of the Retropropulsion Reentry Burn of Vertically Landing Launchers." Journal of Spacecraft and Rockets. 60(6): 1939-1953. https://arc.aiaa.org/doi/10.2514/1.A35647 (2023) Accessed 10 November 2023
7. Marwege, A., Kirchheck, D., Klevanski, J. *et al.* Hypersonic retro propulsion for reusable launch vehicles tested in the H2K wind tunnel. *CEAS Space J* **14**, 473–499 https://link.springer.com/article/10.1007/s12567-022-00457-w (2022). Accessed 10 November 2023
8. SpaceX. NROL-76 Launch Webcast. https://www.youtube.com/watch?v=EzQpkQ1etdA&ab_channel=SpaceX (2017) Accessed 10 November 2023

